EXPERIMENTAL AND NUMERICAL CHARACTERIZATION OF HIGH TEMPERATURE DEFORMATION BEHAVIOR OF 347H STAINLESS STEEL

Jobin K. Joy, A. Rovinelli, M. Arul Kumar, R.A. Lebensohn, L. Capolungo
Los Alamos National Laboratory, Los Alamos, NM,USA

Q.Q. Ren, Y. Yamamoto, J.D. Poplawsky
Oak Ridge National Laboratory, Oak Ridge, TN, USA

M. Detrois, P. Jablonski
National Energy Technology Laboratory, Albany, OR, USA

ABSTRACT

The plasticity and thermal creep response of 347H stainless steel under uniaxial tensile conditions has been studied as a function of temperature. Strain rate-controlled uniaxial tensile tests at strain rates of ~10^{-4} s^{-1} for temperatures ranging from 100°C to 750°C, and tensile creep tests at 600°C, 650°C, 700°C and 750°C for different stress levels were performed. These experiments were used for calibration and validation of a novel integrated mechanistic constitutive model able to handle arbitrary loading conditions with explicit stress and temperature dependence. The constitutive model has been numerically implemented in a full-field elasto-viscoplastic Fast Fourier Transform (EVPFFT) framework for polycrystalline microstructures. Thermally activated dislocation glide and climb, and vacancy diffusional creep are the concurrent mechanisms considered in the model. The heterogenous distribution of internal stresses within a single crystal material point is accounted for, as well as the effect of precipitates, interstitial and substitutional solute atoms on dislocation motion. The model has been calibrated, and its predictions validated against the experimental response of 347H steel. Based on predictions of the validated model, synthetic Ashby-Weertman deformation mechanisms maps were calculated for 347H steel, allowing a deeper understanding of the effect of microstructure on the activation of different creep mechanisms.

INTRODUCTION

Austenitic stainless steels are widely used in automotive and energy sectors, including nuclear and fossil energy industries. In many applications, the material is typically subjected to high temperature and low-to-moderate stresses [1-3]. Under these conditions, the dimensional changes of the structural components are mostly due to thermal creep. Thus, the development of a modeling framework to understand and predict thermal creep mechanisms, and the relationship to the mechanical properties, is important in estimating the performance and life of components in service. The thermal creep response and the associated microstructure evolution of stainless steels have been characterized experimentally in many studies [4-7]. However, microstructure-sensitive material modeling has received less attention. Indeed, most of the available modeling frameworks are empirical and only capable of predicting the steady-state creep response [6, 7]. In actual service conditions, materials often experience sudden changes in mechanical loading and temperature that lead to significant transient behaviors. In addition, the material's mechanical relaxation during creep is governed by the initial microstructure and its evolution, and thus, it is highly sensitive to the thermo-mechanical processing history.

Microstructure-informed constitutive models are necessary to capture the contribution of different mechanisms to the deformation behavior. This requires an understanding of the effects of microstructure features of the material on deformation behavior. These features are intimately connected to composition. For example, in austenitic stainless steels (e.g., SS347), Nb acts as a

stronger carbide former compared to Cr [8]. The addition of Nb to stainless steel (SS) develops NbC carbides when solution annealed and aged, and prevents grain boundary precipitation [8]. Most NbC carbides are formed in the grain interior, and thus, improves tensile and creep strength [5]. In addition, the temperature and duration of subsequent heat treatments control the type and density of precipitates. For instance, ageing of SS347 at 650°C and 750°C resulted in no precipitates at the grain boundaries, whereas solution annealing at 1100°C-1300°C followed by ageing results in Cr-rich carbides at the grain boundaries [8]. The addition of B, N and Ce also enhances the creep life of SS347H [4]. The formation of B-containing precipitates at the grain boundaries lowers the steady state creep rate and increases creep life. The addition of Ce removes O which leads to longer creep life. Finally, the addition of N contributes to solid solution strengthening of the matrix and NbC precipitate formation and strengthening, thereby helping increase tensile and creep strength while increasing creep life.

Recently, a mechanistic constitutive model was developed to capture the thermal and irradiation creep responses of ferritic steels in Wen et al. [9, 10], where the temperature dependence is explicitly expressed in the constitutive laws of the different deformation mechanisms. This facilitates prediction of the creep response of steels for a wider range of stress and temperature without recalibration [11]. However, this model was implemented within a mean-field homogenization framework for polycrystal plasticity and creep, which only provides the values of the average stress and strain (and strain rate) in the grains. More critically, the treatment of dislocation precipitate interactions in Wen et al.[9, 10] did not account for the effective precipitate size due to dislocation-precipitate interaction.

In this work, a physics-based constitutive laws have been improved and subsequently implemented within the full-field elasto-viscoplastic Fast Fourier Transform (EVPFFT) framework to simulate the thermal creep response of SS347H. Dislocation glide, dislocation climb, and vacancy diffusion processes are considered with explicit stress and temperature dependence. The framework is employed to describe the internal stress fluctuations due to dislocations interaction. To calibrate and validate the model, an experimental campaign was completed to measure the uniaxial stress-strain response as a function of temperature and the creep response at different stresses and temperatures of SS347H. The resulting model has been applied to simulate both uniaxial strain rate-controlled and thermal creep and compared against the experimental data. Subsequently, using the calibrated model, creep experiments were simulated for a wider range of stress and temperatures, which allowed us to calculate newly proposed *synthetic Ashby-Weertman deformation mechanisms maps* for 347H steel. The predicted deformation mechanisms map suggests that the power-law exponent, which is commonly used to identify the dominant deformation mechanisms, cannot be employed to uniquely distinguish the deformation regimes. The developed microstructure-sensitive model along with the new insights on the deformation mechanisms will be useful for the designing of creep-resistant materials for next generation power plants and automotive applications.

EXPERIMENTS

The SS347H used in the experimental campaign was manufactured at National Energy Technology Laboratory (NETL) following a conventional cast and wrought processing route. Vacuum induction melting (VIM) was employed to form ~8 kg ingots from high purity, industry grade, stock materials, targeting the composition of 347H (UNS 34709) specified in ASTM A240/240M. Note: The initial stainless-steel variants were formulated without intentional additions of B and N. Following solidification, the ingots were homogenized following a computationally designed homogenization heat treatment cycle to reduce residual elemental inhomogeneity to below 1% [12]. The homogenization heat treatment cycle consisted of a one-hour exposure at 1140°C followed by a twelve-hour exposure at 1225°C which was followed by forced Argon gas fan cooling to room temperature. After preparation of the surface of the ingots, thermomechanical processing (TMP) was performed. The TMP process consisted of the following steps: hot forging followed by hot

rolling in incremental steps at 1150°C with reheat between the steps to produce plates measuring approximately 10 mm in thickness with a recrystallized equiaxed grain structure. The last step was followed by an annealing heat treatment at 1100°C for 5 min followed by air cooling.

Tension and creep testing were performed using specimens machined from the 10 mm thick plates. The tensile axis was parallel to the rolling direction. The specimens consisted of reduced gage cylindrical bars measuring 76.2 mm in overall length, 10 mm in overall diameter, and with ANSI 3/8×16 threaded ends. The reduced gauge section measured 31.75 mm in length and 6.25 mm in diameter. Tensile testing was conducted following the ASTM E8 standard on an electro-mechanical load-frame using a cross-head displacement of 0.127 mm/min until ~1.2% elongation was reached, at which point the extensometer was removed and the cross-head displacement increased to 1.27 mm/min until failure. Tension testing was performed at room temperature, 100, 200, 300, 400, 500, 550, 600, 650, 700, 750, and 800°C. Uni-axial tensile creep-rupture testing was performed according to ASTM E139 using constant load creep frames. The creep strain was measured using a linear variable differential transformer (LVDT) displacement transducer. Testing was performed isothermally in the temperature range of 600 to 800°C for applied stresses of 40 to 265 MPa.

CONSTITUTIVE MODEL

The advanced mechanistic constitutive model presented here is based on the studies in [9-11]. The plastic deformation of the material is accommodated by dislocation glide, dislocation climb, and vacancy diffusion mediated processes. Thus, the plastic strain rate is expressed as:

$$\dot{\varepsilon}^p = \dot{\varepsilon}^d + \dot{\varepsilon}^c + \dot{\varepsilon}^{diff} \tag{1}$$

where $\dot{\varepsilon}^d$, $\dot{\varepsilon}^c$ and $\dot{\varepsilon}^{diff}$ are the plastic strain rates accommodated by dislocation glide, dislocation climb, and diffusional creep processes, respectively. The strain rates due to dislocation motion can be written as the sum of the mean shear/climb rates over all active systems at each material point:

$$\dot{\varepsilon}^d = \sum_s m_{ij}^s \bar{\dot{\gamma}}^s \quad \text{and} \quad \dot{\varepsilon}^c = \sum_s c_{ij}^s \bar{\dot{\beta}}^s \tag{2}$$

Here $\bar{\dot{\gamma}}$ and $\bar{\dot{\beta}}$ denote the mean shear and climb rates, respectively. m^s is the symmetric part of the Schmid tensor. $c = (b^s \otimes b^s)$ is the climb tensor for edge dislocations .

Following Wang et al. [13] the response of each material point (representing single crystal grains in Wang et al.'s case, and single crystals voxels here) accounts for the internal stress distribution to allow considering sub-material point internal stresses associated with dislocations. Accordingly, the mean shear rate of the slip system s in the voxel is expressed as:

$$\bar{\dot{\gamma}}^s = \int_{-\infty}^{\infty} \dot{\gamma}^s(\tau^s)\ P(\tau^s - \bar{\tau}^s) d\tau^s \tag{3}$$

where $\dot{\gamma}^s$ is the shear rate of one sub-material point. τ^s is the local resolved shear stress. $\bar{\tau}^s = \sigma : m^s$ denotes the mean resolved shear stress in one grain. Notice that this law applies to the climb rate as well:

$$\bar{\dot{\beta}}^s = \int_{-\infty}^{\infty} \dot{\beta}^s(\tau^s_{climb})\ P(\tau^s_{climb} - \bar{\tau}^s_{climb}) d\tau^s_{climb} \tag{4}$$

with τ^s_{climb} and $\bar{\tau}^s_{climb} = \sigma : c^s$, being the local and global resolved climb stress, respectively. Note that the internal stress distributions can be related to the dislocation content [14]. Therefore, the probability distribution function $P(\tau^s - \bar{\tau}^s)$, representing the volume fraction of sub-material points with τ^s, is written as:

$$P(\tau^s - \bar{\tau}^s) = \frac{1}{V\sqrt{2\pi}} \exp\left(-\frac{(\tau^s - \bar{\tau}^s)^2}{2V^2}\right) \tag{5}$$

Here V is the distribution standard deviation, and it is expressed as,

$$V = \eta\sqrt{\rho_{cell} + \rho_{cw}} \tag{6}$$

Where $\eta \sim 10^{-7}$ MPa m is an effective scaling coefficient. ρ_{cell} and ρ_{cw} are the total dislocation densities in the cell (subgrain) interior and in the cell walls (subgrain boundaries), respectively.

Dislocation glide

Inevitably, dislocations glide is hindered by various microstructural obstacles. Our model considers the following obstacles to dislocation motion: precipitates, solute atoms, and dislocation junctions. Depending on the applied load and the threshold shear stress, dislocations may undergo continuous glide or delayed glide. The local shear rate on slip system s is expressed using the Orowan equation:

$$\dot{\gamma}^s = \rho^s_{cell,S} b^s v^s \,.\, \mathrm{sign}(\tau^s) \tag{7}$$

where b^s is the magnitude of the Burgers vector, $\rho^s_{cell,S}$ and v^s are the density and velocity of slip dislocations and $\mathrm{sign}(\tau^s)$ enforces the direction of the shear rate to be the same as the direction of glide. The dislocation velocity can be determined from the mean spacing between obstacles (dislocation mean free path, λ^s) and the time a dislocation spends traveling between obstacles, given by the sum of the waiting time at obstacles (t^s_w) and the travel time within the interspacing (t^s_t):

$$v^s = \frac{\lambda^s}{t^s_w + t^s_t} \tag{8}$$

The travel time can be expressed as: $t^s_t = \frac{\lambda^s}{v_t}$, where v_t denotes the dislocation velocity (i.e., the time to travel between obstacles), which is assumed to be same as the shear wave velocity, $C_s = \sqrt{\mu/\rho_0}$. Thus, the travel time is approximated as, $t^s_t = \frac{\lambda^s}{C_s}$.

The waiting time in Eq. (8) depends on the type and spatial distribution of obstacles present in the microstructure. In the three considered types of obstacles (i.e., precipitates, solute atoms, and dislocations), only precipitates and dislocations are explicitly considered when calculating the waiting time. Therefore, the mean wait time is expressed as,

$$t^s_w = P^s_\rho t^s_{w,\rho} + \sum_i^{n_P} P^s_{P_i} t^s_{w,P_i} \tag{9}$$

where $P^s_\rho = \frac{\lambda_s}{\lambda^s_\rho}$ and $P^s_{P_i} = \frac{\lambda_s}{\lambda^s_{P_i}}$ denote the probability that a dislocation encounters other dislocations and precipitate-type obstacles, respectively, and n_P is the number of precipitate-type obstacles like MX and $M_{23}C_6$. Dislocations may bypass obstacles, either via the Orowan mechanism or climb processes. Thus, the effective waiting time of a dislocation at an obstacle is written as,

$$\frac{1}{t^s_{w,i}} = \frac{1}{t^{s(O)}_{w,i}} + \frac{1}{t^{s(c)}_{w,i}} \tag{10}$$

where $t^{s(O)}_{w,i}$ and $t^{s(c)}_{w,i}$ represent the waiting time for the Orowan looping and climb process, respectively, with i refering to either dislocation or precipitate-type obstacle. Following Kocks-type activation enthalpy law [15], for both dislocation and precipitate-type obstacles, the wait time for Orowan looping is written as,

$$t^{s(O)}_{w,i} = \begin{cases} \frac{1}{\nu^s_{a,i}} \exp\left(\frac{\Delta G_{0,i}}{kT}\left(1 - \left(\left|\tau^s_{\mathrm{eff}}\right| / \tau^s_c\right)^p\right)^q\right) & \text{if } |\tau^s_{\mathrm{eff}}| < \tau^s_c \\ 0 & \text{if } |\tau^s_{\mathrm{eff}}| \geq \tau^s_c \end{cases} \tag{11}$$

$\Delta G_{0,i}$ is the thermal activation energy without any external stress for an obstacle i. k is Boltzmann constant. T is the absolute temperature. $p(0 < p \leq 1)$ and $q(1 < q \leq 2)$ are the exponent parameters related to the shape of the obstacles resistance profile [15]. $\nu_{a,i}^{s}$ is the effective attack frequency associated with obstacle i. τ_c^s and τ_{eff}^s refer to the critical resolved shear stress (CRSS) and the available effective driving stress for dislocation motion, respectively.

The dislocation *mean free path*, λ^s, used in Eq. (8), is a combination of the dislocation interspacing, λ_ρ^s, the precipitate interspacing, λ_P^s and the sub-grain size λ_{sg}, and is expressed as:

$$\left(1/\lambda^s\right) = \left(1/\lambda_\rho^s\right) + \left(1/\lambda_{sg}^s\right) + \sum_i^{n_P} \left(1/\lambda_{P_i}^s\right) \tag{12}$$

In addition to the intrinsic frictional resistance, the presence of precipitates, solute atoms and dislocations in the cell wall can contribute the CRSS. The net effect of these strengthening mechanisms is expressed using a non-linear superposition law.

$$\tau_c^s = \tau_0^s + \left\| \tau_{CW}^s, \tau_{L,sub}, \tau_{L,int}, \sum_i \tau_{P_i}^s \right\| \tag{13}$$

In Eq. (13), τ_0^s, τ_{CW}^s, $\tau_{L,sub}$, $\tau_{L,int}$ and $\tau_{P_i}^s$ refer to the friction stress, the strengthening due to cell wall, the effect of solute strengthening at substitutional sites, the effects of solute strengthening at interstitial sites and the strengthening due to precipitates of type I, respectively on slip system s, and '‖ ‖' is the second norm. Following the classical work of Labusch and Nabarro [16, 17], the solid solution strengthening due to substitutional solute atom is given as:

$$\tau_{L,sub} = K_{sub} \mu c_{sub}^{\frac{2}{3}} \tag{14}$$

The strengthening due to interstitial solute atoms in steel, for example, C and N, is proportional to the square root of the solute content [18]:

$$\tau_{L,int} = K_{int} \mu c_{int}^{1/2} \tag{15}$$

In the above equations, K_{sub} and K_{int} are the hardening coefficients for substitutional and interstitial solute elements, respectively. The cell wall dislocation density-induced strengthening is written as,

$$\tau_{CW}^s = \mu b^s \sqrt{\sum_s \overline{\alpha}^{ss'} \rho_{cw}^{s'}} \tag{16}$$

Similarly, the strengthening due to precipitate, *i,* is defined as,

$$\tau_{P_i}^s = \alpha_{P_i} \mu b^s \sqrt{N_{P_i} \overline{d}_{P_i}} \tag{17}$$

Effective stress for thermally activated glide process

The effective shear stress, τ_{eff}^s, in Eq. (11) represents the effective driving stress acting on dislocations inside the cells, which can be expressed as:

$$\tau_{\text{eff}}^s = \langle |\tau^s| - \Delta\tau_m^s - \Delta\tau_l^s \rangle \tag{18}$$

where τ^s denotes the local resolved shear stress, and $\Delta\tau_m^s$ and $\Delta\tau_l^s$ are associated with the local reduction in driving force acting on dislocations due to the presence of solute atoms and dislocation line tension, respectively. Atomistic scale studies showed that when an edge dislocation is pinned at obstacles, solute atoms can easily diffuse around the dislocation core [19]. This will effectively increase the stress required for the dislocation to unpin, and in-turn, control the strain rate

sensitivity of the medium. Dislocation core-diffusion is associated with the time for a solute atom to diffuse around the dislocation core, t_d, which modulates the binding energy of the solute atom to the dislocation. The latter is given as:

$$\Delta E^{\text{core}}(t) = \Delta E_{\infty}^{\text{core}} \left(1 - exp\left(-\left({}^{t}/_{t_d}\right)^{\varphi}\right)\right) \tag{19}$$

where $\Delta E_{\infty}^{\text{core}}$ is the saturation value for the binding energy; it is written as,

$$\Delta E_{\infty}^{\text{core}} = c_0 N \Delta \bar{W} \tanh\left({}^{\Delta \bar{W}}/_{2kT}\right) \tag{20}$$

Here, c_0 and N denotes the total solute atom concentration in the bulk, and number of atoms per unit length of dislocation segment, respectively. $\Delta \bar{W}$ refers to the average binding energy difference. Consequently, the drag stress due to diffusion of solute atoms can be written as:

$$\Delta \tau_m^s\left(t_{a,local}^s\right) = \frac{\alpha \Delta E^{\text{core}}\left(t_{a,local}^s\right)}{\bar{w} b^s} \tag{21}$$

$t_{a,local}^s$ is the local aging time (pinning period). α is associated with the energy variation along the dislocation core. $\bar{w}$ denotes the dislocation core width. The term t_d is written as,

$$t_d = \frac{1}{m \nu_0} exp\left(\frac{\Delta H_c - {}^{\Delta \bar{W}}/_{2}}{kT}\right) \tag{22}$$

$\Delta \tau_l^s$ in Eq. (18) is the self-stress resulting from the dislocation curvature (i.e., line tension). The line tension $\Delta \tau_l^s$ can be expressed as the following in terms of the latent hardening matrix ($\bar{\alpha}^{ss\prime}$) and $\rho_{cell}^{s\prime}$.

$$\Delta \tau_l^s = \mu b^s \sqrt{\sum_{s} \bar{\alpha}^{ss\prime} \rho_{cell}^{s\prime}} \tag{23}$$

Following Picu [20], who showed that solute atoms may also increase the effective dislocation-dislocation junction strength, $\Delta \tau_l^s$ is expected to depend on the aging history. Therefore, the effective latent hardening matrix $\bar{\alpha}^{ss\prime}$ here is a function of binding energy $\Delta E_{\infty}^{\text{core}}$.

Dislocation climb

Dislocation climb is the deformation mechanism by which dislocation segments containing edge character move perpendicular to their slip plane. Similar in form to Eq. (7), the local climb rate can be expressed as an *Orowan-type* equation. Notice that in this model only edge dislocations contribute to the climb rate:

$$\dot{\beta}^s = \rho_{cell,edge}^s b^s v_{climb}^s \tag{24}$$

Here, $\rho_{cell,edge}^s$ denotes the edge dislocation density. v_{climb}^s represents the climb velocity, which depends on the net flux of point defects I^s to and from the dislocation,

$$v_{climb}^s = \frac{\Omega}{b} I^s = \frac{\Omega}{b} z_v^s D_v (c_v^0 - c_v^{sat}) \tag{25}$$

Here, $\Omega \approx b^3$ is the atomic volume; z_v^s represents the capture efficiency for vacancies. D_v denotes the vacancy diffusivity. c_v^0 and c_v^{sat} refer to the vacancy concentration around a dislocation at thermal equilibrium and the saturation vacancy concentration, respectively. The former vacancy concentration depends on the local stress and temperature, and thus, $c_v^0 = c_v^{th} \exp\left(\frac{\Omega \bar{\tau}_{climb}^s}{kT}\right)$ [21]. $\bar{\tau}_{climb}^s$ is the Piola-Kirchoff force for climb, and c_v^{th} is the thermal equilibrium vacancy concentration. c_v^{sat} is assumed to be the same as the c_v^{th} because of thermal equilibrium. The thermal equilibrium vacancy number concentration in the bulk is generally written as [22],

$$c_v^{th} = \frac{n}{N} = \exp\left(\frac{S_f}{k}\right) \exp\left(\frac{-E_f}{kT}\right) \tag{26}$$

where E_f and s_f refer to the vacancy formation energy and entropy, respectively. The n and N correspond to number of vacancies and number of atoms on the lattice sites, respectively.

Dislocation density evolution

The evolution of dislocation density governs the shear and climb rate on individual slip systems. The dislocation density evolution law developed by [9] is employed here. The dislocation content can be divided into two populations: dislocations in the cell (subgrain) and in the cell walls (subgrain boundary). The evolution of the dislocation density in the cell is expressed as:

$$\dot{\rho}^s_{\text{cell}} = \dot{\rho}^{s,+}_{\text{cell,g}} - \dot{\rho}^{s,-}_{\text{cell,a}} - \dot{\rho}^{s,-}_{\text{cell,trap}} \tag{27}$$

where $\dot{\rho}^{s,+}_{\text{cell,g}}$, $\dot{\rho}^{s,-}_{\text{cell,a}}$, and $\dot{\rho}^{s,-}_{\text{cell,trap}}$ denote the dislocation generation, dynamic recovery and trapping at the subgrain boundaries. The dislocation generation rate is associated with the area swept by the moving dislocations and is expressed as [23]:

$$\dot{\rho}^{s,+}_{\text{cell,g}} = \frac{k_1}{b\lambda^s}|\bar{\dot{\gamma}}^s| \tag{28}$$

where $\frac{\lambda^s}{k_1}$ is the effective mean free path. Following the work of Estrin [24], dynamic recovery is written as:

$$\dot{\rho}^{s,-}_{\text{cell,a}} = k_2 \left(\dot{\varepsilon}_0/\dot{\varepsilon}\right)^{1/n_0} \rho^s_{\text{cell}}|\bar{\dot{\gamma}}^s| \tag{29}$$

where $\dot{\varepsilon}_0$ is a reference strain rate. The dislocation trapping rate at the subgrain boundaries is related to the subgrain size λ_{sg}:

$$\dot{\rho}^{s,-}_{\text{cell,trap}} = \frac{k_3}{\lambda_{\text{sg}}}|\bar{\dot{\gamma}}^s| \tag{30}$$

The trapped dislocations will essentially become part of the wall structure. Meanwhile, the dislocations in the cell wall will also annihilate. Thus, the annihilation rate ρ^s_{cw} can be written as:

$$\dot{\rho}^s_{\text{cw}} = \dot{\rho}^{s,-}_{\text{cell,trap}} - \dot{\rho}^{s,-}_{\text{cw,a}} \tag{31}$$

EVPFFT Framework

We utilize a full-field EVPFFT framework to implement physics-based models to predict the plastic and thermal creep response of 347H steel for a wide range of temperatures and stress or strain rate conditions. The original FFT-based formulation was developed to study the micromechanical response of composite materials [25], and later adapted [26] to polycrystals, to study the effective and local response in this class of materials, associated with the heterogeneity in the spatial distribution of crystal orientations, with inherently directional mechanical properties. The FFT-based formulation for polycrystals has been extended to different deformation regimes, like elasticity [27], incompressible viscoplasticity [26], dilatational viscoplasticity [28], infinitesimal elasto-viscoplasticity [29] and finite elasto-viscoplasticity [30] and strain-gradient plasticity [31]. The numerical scheme for infinitesimal elasto-viscoplasticity [29] is employed for solving the mechanical response of the material from its 3D Representative Volume Elements (RVEs).

RESULTS AND DISCUSSION

To calibrate and validate the new mechanistic constitutive model, uniaxial strain rate-controlled tensile tests at different temperatures, and constant load creep tests for a range of stresses, for different temperatures are considered. As mentioned in the experiments, the initial material used for the experimental tests is annealed and fully recrystallized, and thus, it possessed an equiaxed

grain structure with uniform distribution of crystal orientations. To emulate this microstructure, the EVPFFT unit cell is discretized into 32x32x32 voxels with almost equiaxed grain structure. The initial texture is approximated by 50 randomly oriented grains. The initial dislocation content, both in the cells and cell-walls is not accurately known. At the same time, unlike ferritic steels (e.g., Grade 91) [8], austenitic stainless streels do not tend to contain dislocation cell-structures after annealing. Therefore, initial values of ρ_{cell} and ρ_{CW} to be 5×10^{12} m^{-2} and 1×10^{11} m^{-2}, respectively, were adopted. Only NbC type precipitates are present inside the grain matrix. The size and density of NbC precipitates are: 330.0 nm and $3.5 \times 10^{17} m^{-3}$.

First, the uniaxial stress-strain response of SS347H as a function of temperature is discussed. Experimental tensile curves for temperatures ranging from 100°C to 750°C are shown in *Figure 1* (a) in dashed lines. The imposed strain rate is 0.84×10^{-4} s^{-1}. As expected, increasing temperature decreases the yield stress and strain hardening. However, the decrease in the strain hardening rate with temperature is not constant. The stress-strain responses predicted with EVPFFT model are shown in *Figure 1*(a) as solid lines. To calibrate the model parameters, the stress-strain curves at 300°C, 400°C and 600°C were used. The curves for the other four temperatures were reserved for model validation. *Figure 1*(a) clearly shows that the model captures the temperature dependence of yield stress and strain hardening behavior. For all temperature cases, beyond the elastic regime, the plastic deformation is mostly accommodated by dislocation glide.

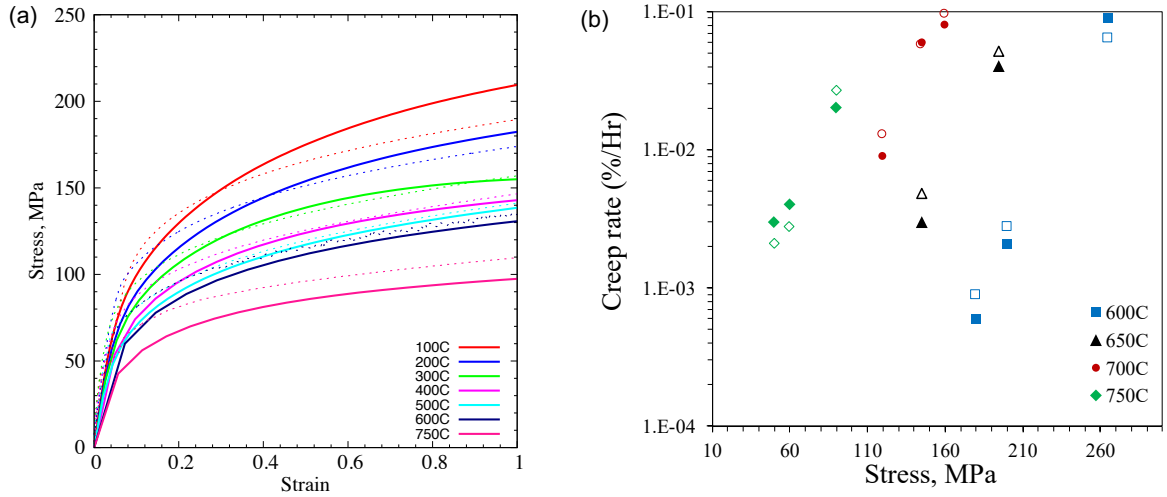

Figure 1: (a) Experimental (dashed lines) and predicted (solid lines) uniaxial stress-strain response of SS347H as a function of temperature. (b) Variation in -the steady state creep rate as a function of stress for four different temperatures (600 ℃, 650 ℃, 700 ℃ and 750 ℃). Hollow and solid symbols correspond to the experiments and model predictions, respectively.

Creep tests were also performed, at four different temperatures: 600°C, 650°C, 700°C and 750°C. The imposed stress values are different for the different temperatures. Experimentally measured steady-state creep rate is plotted (hollow symbols) as a function of the imposed stress for different temperatures in *Figure 1* (b). Both the temperature and imposed stress strongly influence the creep rate. Importantly, the steady state creep rates vary over three orders of magnitude for a temperature range of only 150°C. Similarly to the previous case, four creep cases were considered for model calibration: 600°C/180 MPa, 600°C/265 MPa, 700°C/145 MPa, and 750°C/60 MPa. The other seven cases were reserved for model validation. The predicted steady state creep rates (solid symbols) for the four temperatures are shown in Figure 1(b). First, the model correctly captures the complex combined effect of stress and temperature on the creep responses. However, the model slightly over- and under-estimates the creep rate for higher and lower temperatures, respectively, for lower stresses and vice versa for higher stresses.

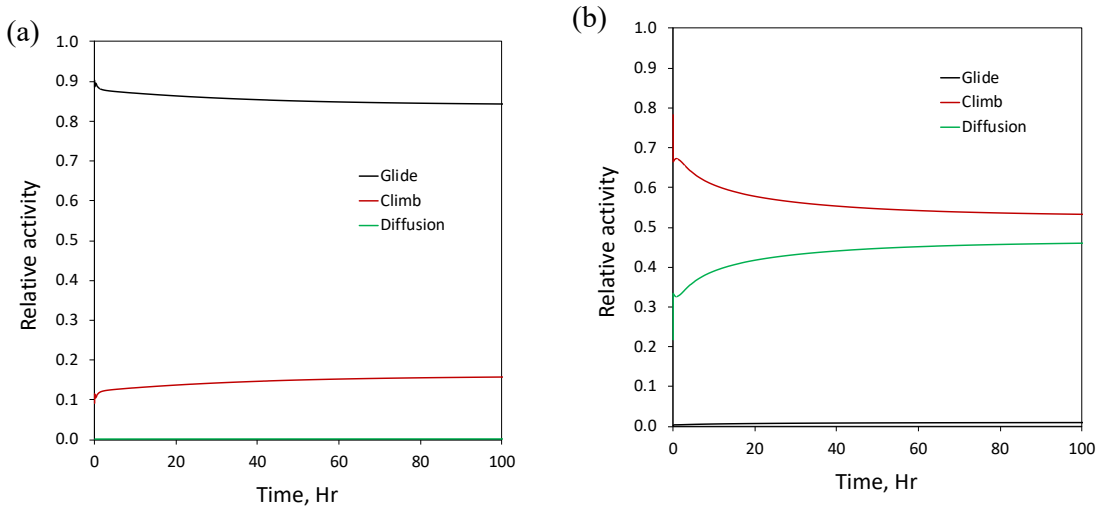

Figure 2: Relative contribution of dislocation glide, dislocation climb and diffusional creep to the predicted thermal creep response for (a) 600 ℃ and 180 MPa and (b) 750 ℃ and 60 MPa.

To further understand the predicted creep responses, the relative contribution of different deformation mechanisms is analyzed here. These are calculated as the ratio of the plastic strain rate due to a deformation mode over the total plastic strain rate along the loading direction. *Figure **2*** shows the relative activity of dislocation glide, dislocation climb and diffusional creep for two representative creep tests: 600°C and 180 MPa, and 750°C and 60 MPa. In the former case, the imposed stress is higher than the yield stress, whereas in the latter case, the imposed stress is slightly lower. For the case of 600°C and 180 MPa, the creep deformation is accommodated by a combination of dislocation glide and dislocation climb. Among these two modes, dislocation glide (~85%) accommodated most of the deformation compared to dislocation climb (~15%). The contribution from diffusional creep is negligible at 600°C and 180 MPa. In the case of creep at 750°C and 60 MPa, creep deformation is mainly accommodated by dislocation climb and diffusional creep, and not so much by dislocation glide. Dislocation climb and diffusional creep accommodate around 55% and 45% of the deformation, respectively, whereas dislocation glide accommodates less than 2% of the total plastic deformation.

Ashby-Weertman deformation mechanisms map

Using the EVPFFT implementation of the mechanistic constitutive model of thermal creep, synthetic Ashby-Weertman deformation mechanisms maps for SS347H were produced (*Figure 3)*. To cover the stress-temperature range shown in *Figure 3,* we performed a total of 195 creep simulations, covering the entire mapping region uniformly. For all simulations, only uniaxial tensile stress responses were considered. During creep, the three plastic deformation mechanisms (glide, climb and diffusion) are activated and contribute to deformation/creep rate. Depending on stress and temperature, one specific mechanism may dominate the creep response compared to the other two. To build the synthetic maps, a plastic deformation mode is assigned as the dominant mechanism for each stress and temperature condition, if it contributes more than 50% of the overall deformation. Based on this criterion, a synthetic map for SS347H is shown in Figure 5. The color bar represents the predicted steady-state creep rate. The temperature ranges from 550°C to 800°C; and the stress ranges from 20 MPa to 300 MPa. Generally, the deformation maps are presented in the space of homologous temperature and shear modulus-normalized stress [32]. The corresponding ranges of homologous temperature $\left({}^{T}/_{T_m}\,; T_m = 1783K\right)$ and normalized stress $\left({}^{\sigma}/_{\mu}, \mu = 77.028GPa\right)$ for the map shown in Figure 5 is 0.461 to 0.6; and 2.5×10^{-4} to 3.9×10^{-3}, respectively.

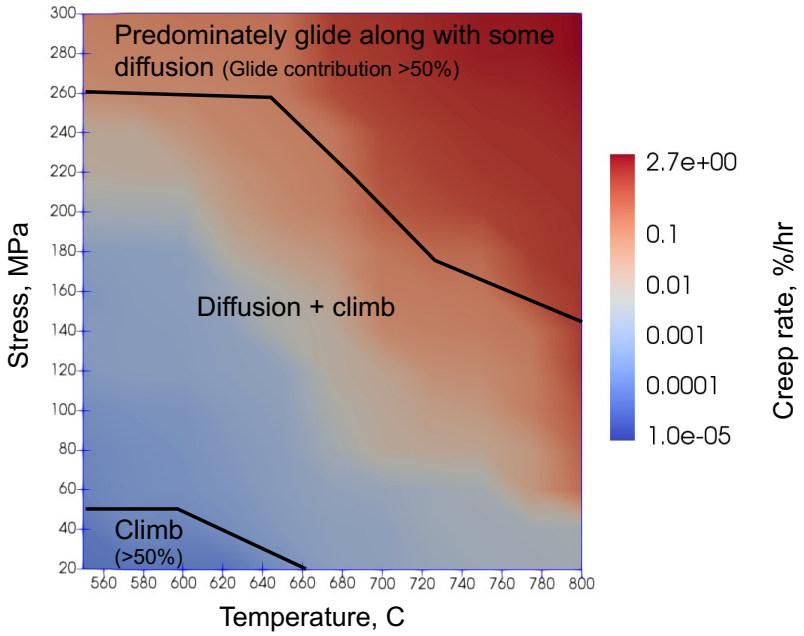

Figure 3: Ashby-Weertman deformation mechanisms map of SS347H in the stress-temperature space.

This synthetic deformation mechanisms map suggests that for lower stresses and lower temperature, dislocation climb dominates the creep response as it accommodates more than 50% of the creep deformation. For higher stresses and higher temperatures (mostly top and top-right region of the map), dislocation glide dominates the deformation along with a noticeable amount of diffusional creep. Interestingly, for moderate stress and temperature, diffusional creep and dislocation climb share the accommodation of creep deformation. In this regime, none of the deformation modes contributes more than 50% to deformation.

Conversely, the typical deformation mechanisms map is divided into three main regimes namely plasticity, diffusional flow and power law creep [32]. In the plasticity regime, the material undergoes work hardening, whereas in the diffusional and power-law creep regimes material undergoes relaxation until it eventually reaches a steady-state. The diffusional flow and power-law creep regimes are identified using an exponent, n, of the constitutive law which relates the shear rate to the stress: $\dot{\gamma} \propto \left({}^{\sigma}/_{\mu}\right)^{n}$. For the diffusional flow regime, the value of n is one and it considers both the lattice diffusion (i.e., Nabarro-Hearing creep) and grain boundary diffusion (i.e., Coble creep). In this work, the diffusional regime also describes both lattice and grain boundary diffusion processes. In the power-law regime, the inverse of the strain rate-sensitivity exponent is greater than one. Its value is conditioned by the relative activities of all possible dislocation mediated processes, like pure dislocation glide, glide-assisted-by-climb, which is controlled by lattice-diffusion and/or core-diffusion, and the transition from climb-and-glide to pure glide. As a result, most of the deformation mechanisms map is occupied by the power-law regime, and the other regimes cannot simply be isolated, i.e., pure glide, pure climb and climb-and-glide.

However, using the proposed model, the glide-controlled regime can be differentiated from the climb-controlled regime. Importantly, the model predicts the pure climb regime coincides with the diffusional flow regime in the conventional deformation mechanisms maps. Also, the results suggest that the diffusional flow regime cannot be isolated from the climb-dominated regime. Thus, the power-law exponent cannot be used to uniquely distinguish the diffusional flow regime from the power-law regime, which is mainly a climb-controlled process. The new insights and the developed deformation mechanism map will aid in building creep resistant designs with the improved ability to identify the dominant mechanism at the specified creep condition.

CONCLUSIONS

In this work, the high-temperature deformation behavior of SS347H has been systematically investigated using experiments and numerical modeling. Strain rate-controlled uniaxial tensile tests and creep tests were conducted at different temperatures and stresses. To understand the measured stress-strain and creep responses, a physics-based constitutive model with explicit stress and temperature dependence has been developed within the EVPFFT framework. In the model, plastic deformation is accommodated by a combination of thermally-activated dislocation glide/dislocation climb and vacancy diffusional creep.

The new model has been calibrated and its predictions were validated against experimentally measured uniaxial tensile stress-strain and creep curves. The model predictions agree well with the experimental observations. The relative roles of different plastic deformation mechanisms such as dislocation glide, dislocation climb and diffusional creep, were discussed. EVPFFT simulations of thermal creep were performed for a wide range of stresses and temperatures to construct synthetic Ashby-Weertman deformation mechanisms maps for SS347H. The predicted deformation mechanisms map suggests that the power-law exponent, which is commonly used to identify the dominant deformation mechanisms, cannot be employed to uniquely single out a dominant mechanism.

Further, variations of the initial microstructure (in terms of initial dislocation densities) have been studied to ascertain its effect on steady-state creep rates and general deformation mechanisms map features. We observed that a decrease in initial dislocation density decreases the steady-state creep rate and the relative contribution from glide and climb mechanisms. Specifically, model calculations showed that the sensitivity of the creep response to the initial state of the microstructure (described simply by the dislocation content) will vary non uniformly over given temperature and stress ranges. Indeed, diffusion-dominated regions will be far less sensitive to dislocation content than regions in which dislocation glide/climb are activated.

ACKNOWLEDGMENTS

This work was funded by US Department of Energy, FE program XMAT.

REFERENCES

[1] P.J. Maziasz, J.T. Busby, Properties of Austenitic Stainless Steels for Nuclear Reactor Applications, in, Oak Ridge National Lab.(ORNL), Oak Ridge, TN (United States), 2012.
[2] Y. Inoue, M. Kikuchi, Present and future trends of stainless steel for automotive exhaust system, High-temperature, 950 (2003) 750.
[3] D. Gandy, J. Shingledecker, R. Viswanathan, Fossil materials research at EPRI, in: Proceedings 6th International Conference on Advances in materials technology for fossil power plants, 2011, pp. 65-71.
[4] Y. Xu, H. Nie, J. Li, X. Xiao, C. Zhu, J. Zhao, Growth of creep life of type-347H austenitic stainless steel by micro-alloying elements, Materials Science and Engineering: A, 528 (2010) 643-649.
[5] Y. Li, Y. Liu, C. Liu, C. Li, Y. Huang, H. Li, W. Li, Carbide dissolution and precipitation in cold-rolled type 347H austenitic heat-resistant steel, Materials Letters, 189 (2017) 70-73.
[6] M. Spindler, The prediction of creep damage in Type 347 weld metal: part II creep fatigue tests, International journal of pressure vessels and piping, 82 (2005) 185-194.
[7] M. Spindler, The multiaxial and uniaxial creep ductility of Type 304 steel as a function of stress and strain rate, Materials at high Temperatures, 21 (2004) 47-54.
[8] K. Chandra, V. Kain, R. Tewari, Microstructural and electrochemical characterisation of heat-treated 347 stainless steel with different phases, Corrosion science, 67 (2013) 118-129.
[9] W. Wen, L. Capolungo, A. Patra, C.N. Tome, A Physics-Based Crystallographic Modeling Framework for Describing the Thermal Creep Behavior of Fe-Cr Alloys, Metall Mater Trans A, 48a (2017) 2603-2617.

[10] W. Wen, A. Kohnert, M.A. Kumar, L. Capolungo, C.N. Tomé, Mechanism-based modeling of thermal and irradiation creep behavior: An application to ferritic/martensitic HT9 steel, International Journal of Plasticity, 126 (2020) 102633.
[11] L.B. Munday, S.L. Dhulipala, A. Casagranda, S.A. Pitts, B.W. Spencer, A. Tallman, M.A. Kumar, C. Matthews, M. Messner, A. Chakraborty, Multiscale-Informed Modeling of High Temperature Component Response with Uncertainty Quantification, in, Idaho National Lab.(INL), Idaho Falls, ID (United States), 2020.
[12] P.D. Jablonski, J.A. Hawk, Homogenizing advanced alloys: thermodynamic and kinetic simulations followed by experimental results, Journal of Materials Engineering and Performance, 26 (2017) 4-13.
[13] H. Wang, L. Capolungo, B. Clausen, C. Tomé, A crystal plasticity model based on transition state theory, International Journal of Plasticity, 93 (2017) 251-268.
[14] I. Groma, F. Székely, Analysis of the asymptotic properties of X-ray line broadening caused by dislocations, Journal of applied crystallography, 33 (2000) 1329-1334.
[15] U.F. Kocks, A.S. Argon, M.F. Ashby, Thermodynamics and kinetics of slip, Progress in materials science, 19 (1975) 171-229.
[16] R. Labusch, A statistical theory of solid solution hardening, physica status solidi (b), 41 (1970) 659-669.
[17] F. Nabarro, The theory of solution hardening, Philosophical magazine, 35 (1977) 613-622.
[18] G. Krauss, Martensite in steel: strength and structure, Materials science and engineering: A, 273 (1999) 40-57.
[19] G. Leyson, W. Curtin, Solute strengthening at high temperatures, Modelling and Simulation in Materials Science and Engineering, 24 (2016) 065005.
[20] R. Picu, A mechanism for the negative strain-rate sensitivity of dilute solid solutions, Acta Materialia, 52 (2004) 3447-3458.
[21] J.P. Hirth, J. Lothe, Theory of dislocations, 2nd ed., Krieger Pub. Co., Malabar, FL, 1992.
[22] G.S. Was, Fundamentals of radiation materials science: metals and alloys, Springer, 2016.
[23] W. Wen, M. Borodachenkova, C. Tomé, G. Vincze, E. Rauch, F. Barlat, J. Grácio, Mechanical behavior of low carbon steel subjected to strain path changes: Experiments and modeling, Acta Materialia, 111 (2016) 305-314.
[24] Y. Estrin, Dislocation theory based constitutive modelling: foundations and applications, Journal of Materials Processing Technology, 80 (1998) 33-39.
[25] J. Michel, H. Moulinec, P. Suquet, A computational method based on augmented Lagrangians and fast Fourier Transforms for composites with high contrast, Cmes-Computer Modeling in Engineering & Sciences, 1 (2000) 79-88.
[26] R.A. Lebensohn, N-site modeling of a 3D viscoplastic polycrystal using Fast Fourier Transform, Acta Materialia, 49 (2001) 2723-2737.
[27] R. Brenner, R.A. Lebensohn, O. Castelnau, Elastic anisotropy and yield surface estimates of polycrystals, Int J Solids Struct, 46 (2009) 3018-3026.
[28] R.A. Lebensohn, M.I. Idiart, P.P. Castaneda, P.G. Vincent, Dilatational viscoplasticity of polycrystalline solids with intergranular cavities, Philosophical Magazine, 91 (2011) 3038-3067.
[29] R.A. Lebensohn, A.K. Kanjarla, P. Eisenlohr, An elasto-viscoplastic formulation based on fast Fourier transforms for the prediction of micromechanical fields in polycrystalline materials, International Journal of Plasticity, 32-33 (2012) 59-69.
[30] P. Eisenlohr, M. Diehl, R.A. Lebensohn, F. Roters, A spectral method solution to crystal elasto-viscoplasticity at finite strains, International Journal of Plasticity, 46 (2013) 37-53.
[31] M. Zecevic, R.A. Lebensohn, L. Capolungo, New large-strain FFT-based formulation and its application to model strain localization in nano-metallic laminates and other strongly anisotropic crystalline materials, Mech Mater, 166 (2022).
[32] H.J. Frost, M.F. Ashby, Deformation mechanism maps: the plasticity and creep of metals and ceramics, Pergamon press, 1982.